Published in final edited form as:

Nature. 2018 August ; 560(7719): 509–512. doi:10.1038/s41586-018-0396-4.

Inositol phosphates are assembly co-factors for HIV-1

Robert A. Dick[1,*], **Kaneil K. Zadrozny**[2], **Chaoyi Xu**[3], **Florian K. M. Schur**[4,5], **Terri D. Lyddon**[6], **Clifton L. Ricana**[6], **Jonathan M. Wagner**[2], **Juan R. Perilla**[3], **Barbie K Ganser-Pornillos**[2], **Marc C. Johnson**[6], **Owen Pornillos**[2,*], and **Volker M. Vogt**[1]

[1]Department of Molecular Biology and Genetics, Cornell University, Ithaca, NY

[2]Department of Molecular Physiology and Biological Physics, University of Virginia, Charlottesville, VA

[3]Department of Chemistry and Biochemistry, University of Delaware, Newport, DE

[4]Structural and Computational Biology Unit, EMBL, Heidelberg, Germany

[5]Institute of Science and Technology Austria, Klosterneuburg, Austria

[6]Department of Molecular Microbiology and Immunology, University of Missouri, Columbia, MO

Abstract

Information of the HIV-1 virus particle, a short, 14-amino acid segment called SP1, located in the Gag structural protein[1], plays a critical role. During virus assembly the SP1 peptide and seven preceding residues fold into a six-helix bundle (6HB) that holds together the Gag hexamer and facilitates formation of a curved immature hexagonal lattice underneath the viral membrane[2,3]. Upon completion of assembly and budding, proteolytic cleavage of Gag leads to virus maturation, in which the immature lattice is broken down; the liberated CA domain of Gag then re-assembles into the mature conical capsid that encloses the viral genome and associated enzymes. Folding and proteolysis of the 6HB are critical rate-limiting steps of both Gag assembly and disassembly, and the 6HB is an established target of HIV-1 inhibitors[4,5]. Using a combination of structural and functional analyses, we show here that inositol hexakisphosphate (IP6) facilitates formation of the 6HB and assembly of the immature HIV-1 Gag lattice. IP6 makes ionic contacts with two rings of lysine residues at the center of the Gag hexamer. Proteolytic cleavage then unmasks an alternative binding site, where IP6 interaction promotes assembly of the mature capsid lattice. These studies identify IP6 as a naturally occurring small molecule that promotes both HIV-1 assembly and maturation.

[*]Correspondence to: rad82@cornell.edu, opornillos@virginia.edu. Correspondence and requests for materials should be addressed to rad82@cornell.edu.

Contributions. R.A.D. performed protein purification and *in vitro* assembly. F.K.M.S. did comparative analyses of cryoEM and crystal structure data. K.K.Z, J.M.W., B.K.G-P, and O.P. carried out crystallization trials and structure determination. B.K.G-P. performed 2D cryoEM. J.R.P. and C.X. performed all-atom MD simulations. T.D.L., C.L.R., and M.C.J., performed the cell biology and virology work. The manuscript was written primarily by R.A.D., J.R.P., B.K.G-P., O.P., and V.M.V. The project was originally conceived by R.A.D., with input from all authors throughout experimentation and manuscript preparation.

Competing interests. The authors declare no competing interests.

Inositol hexakisphosphate (IP6) is a highly negatively-charged compound present in all mammalian cells at concentrations of 10–40 μM[6]. Inositol phosphates stimulate *in vitro* assembly of HIV-1 Gag into immature VLPs, with previous data suggesting interactions with both the MA and NC domains[7–9]. To understand how IP6 affects HIV-1 assembly, we used an HIV-1 Gag construct spanning the CA to NC domains and having one extra amino acid residue, Ser, preceding the normal N-terminal Pro at the start of CA (*s*-CANC; Fig. 1a), because this should disfavor formation of the N-terminal β-hairpin that promotes mature assembly[10]. Longer N-terminal extensions of CANC constructs were previously shown to assemble inefficiently into immature VLPs at pH 8, but into mature VLPs at pH 6[1,10]. However, we found that *s*-CANC still formed mature-like particles at both pH values (Fig. 1b). Importantly, the presence of IP6 induced a dramatic switch to formation of spherical, immature VLPs (Fig. 1b,d). At pH 8, even a substoichiometric 1:50 molar ratio of IP6 relative to protein resulted in a ~100-fold increase in immature VLPs (Fig. 1b,c). At pH 6, the IP6 effect was somewhat less dramatic, requiring at least a 1:10 ratio to induce immature assembly (Fig. 1b). We conclude that IP6 imposes an *in vitro* immature assembly phenotype, even under conditions that favor the mature lattice (pH 6).

Other inositol derivatives also promoted *s*-CANC assembly but to a lesser extent, in the order IP3 < IP4 < IP5 < IP6 (Fig. 1e,f), correlating with the number of phosphate groups. Other negatively-charged compounds did not or only marginally promoted assembly (Extended Data Fig. 1). Overall, these results indicate that charge neutralization is a fundamental aspect of IP6-mediated HIV-1 Gag assembly, and that the details of coordination geometry and/or local stereochemistry also are important.

To address the biological importance of IP6 in HIV-1 replication, we generated a knockout cell line in which the gene encoding inositol pentakisphosphate 2-kinase (IPPK), the enzyme responsible for the final step in IP6 synthesis, is ablated (Fig. 1g). Infectious HIV-1 particle production from these knockout cells was reduced 10 to 20-fold (Fig. 1g). We interpret this result to imply a critical role of IP6 in immature and/or mature HIV-1 assembly.

Since the *s*-CANC construct lacks the MA domain, the IP6 effect cannot be dependent on MA, as previously suggested[7–9]. The NC domain also cannot be essential since IP6 still promoted assembly in the absence of nucleic acid (Extended Data Fig. 2a,d). Furthermore, IP6 also promoted formation of abundant immature VLPs from the smaller protein *s*-CASP1, which lacks the NC domain altogether (Fig. 2a and Extended Data Fig. 2b,d). However, deletion of SP1 abrogated the IP6 effect, since IP6 failed to induce assembly of *s*-CA into immature VLPs (Extended Data Fig. 2c).

Both the CA domain of Gag and the mature CA protein are composed of two separately folded sub-domains, CA_{NTD} and CA_{CTD}. To further delimit the site of IP6 action, we removed the N-terminal CA_{NTD} sub-domain to create CA_{CTD}SP1, which makes up the "minimal" Gag hexagonal lattice[3,11]. In the presence but not the absence of IP6, and at physiological pH and ionic strength, CA_{CTD}SP1 formed flat hexagonal crystals by negative stain electron microscopy (Fig. 2b). These crystals had the characteristic immature lattice spacing (Fig. 2c). That *s*-CASP1 formed a spherical lattice while CA_{CTD}SP1 formed a flat lattice suggests that CA_{NTD} provides the contacts necessary for enforcing lattice curvature.

We next determined the structure of $CA_{CTD}SP1$ crystallized in the presence of IP6 (Fig 2d,e; Extended Data Table 1). This revealed a single, 6-fold symmetric density in the middle of the hexameric ring (blue mesh in Fig. 2d-f), indicating that one IP6 molecule binds one $CA_{CTD}SP1$ hexamer. Importantly, this density coincides precisely with an unknown density feature observed in cryoEM maps of the HIV-1 Gag hexamer derived from authentic immature virions[2] (Extended Data Fig. 3). This further supports the idea that IP6 is indeed a cofactor of Gag assembly in cells and is a structural component of the HIV-1 particle.

IP6 is an asymmetric molecule with multiple stereoisomers, the most abundant of which is the *myo* form, with a chair configuration of one axial and five equatorial phosphate groups[12]; this is the most commonly observed stereoisomer in structures of various IP6-binding proteins[13–15]. In our $CA_{CTD}SP1$ structure, the IP6 density is also consistent with the *myo* form, with the axial phosphate pointing towards the 6HB (Fig. 2f). The bound ligand can adopt six energetically equivalent orientations, and the 6-fold symmetric density therefore is the sum of these equivalent positions (Extended Data Fig. 4a). More importantly, the bound IP6 is surrounded by two rings of lysine sidechains – Lys290 (K290) from the major homology region (MHR) loop and Lys359 (K359) from the 6HB (Fig. 2g). In our previous crystal structure of the $CA_{CTD}SP1$ hexamer in the absence of IP6, sidechain densities for these lysines were not visible, implying that these residues were highly flexible[3]. In the current structure, these sidechains are better ordered, and in direct ionic contact through their primary ε-amines with the IP6 phosphate groups (Extended Data Fig. 4b).

Consistent with the structure, we found that K290A and K359A *s*-CANC mutant proteins were 100-fold less responsive to added IP6 (Extended Data Fig. 5a-d). These results further indicate that both lysine rings are required for productive IP6 binding. K290R and K359R mutants had less pronounced defects but still did not respond to IP6 as well as wildtype *s*-CANC, consistent with the high degree of lysine conservation in these positions (99.94% for K290 and 99.84% for K359, http://www.hiv.lanl.gov). Furthermore, the K290A and K359A mutations abolished infectivity (Extended Data Fig. 5e). Thus, optimal HIV-1 assembly in cells appears to require lysines at both positions. Previous studies that examined the effects of the above mutations on virus budding from cells and on virus infectivity correlate well with our findings[16–19].

The above data suggest that IP6 acts by stabilizing the 6HB and promoting formation of the immature Gag hexamer. To test this notion, we examined the dynamic behavior of the $CA_{CTD}SP1$ hexamer by using all-atom molecular dynamics simulations. In the absence of IP6, the 6-fold symmetry of the $CA_{CTD}SP1$ hexamer collapsed after 200 ns and did not recover during the 2 μs of simulation (Extended Data Fig. 6 and Video 1). In contrast, 6-fold symmetry in the presence of IP6 was maintained, particularly at the top of the 6HB, proximal to the IP6-binding site. Other inositol derivatives and mellitic acid (hexacarboxybenzene) also stabilized the 6HB in our simulations, consistent with their ability to also support immature *s*-CANC assembly *in vitro* (Extended Data Fig. 6b,c).

We also examined the effect of IP6 on mature capsid assembly, which is mediated by the CA protein that is generated upon Gag proteolysis. We found that IP6 promoted assembly of

HIV-1 CA into mature-like structures[1,10,20] (Fig. 3a and Extended Data Fig. 7b,d). Compared to immature *s*-CANC assembly, however, higher amounts of IP6 were required (Extended Data Fig. 7b,d). Mellitic acid (Extended Data Fig. 7c,e) and IP5, but not IP4 or IP3 (Extended Data Fig. 7f,g), stimulated mature CA assembly although less potently than IP6.

The mature HIV-1 CA hexamer also contains a positively-charged ring, made up of Arg18 sidechains (Arg150 in Gag numbering)[21,22]. This ring was previously shown to mediate transport of nucleoside triphosphates, which facilitates reverse transcription of the encapsulated genome[23]. We therefore tested if IP6 would promote assembly of the HIV-1 CA R18A mutant, and indeed the results were negative (Fig. 3b). HIV-1 virions harboring this mutation were also non-infectious[17,23] (Extended Data Fig. 5e). We next crystallized the mature CA hexamer in the presence of IP6 (Extended Data Table 1). Although IP6 can bind both above and below the ring (Extended Data Fig. 8), densities were most pronounced in the upper binding site, inside a chamber surrounded by the N-terminal β-hairpins of CA (Fig. 3c-f). Thus, IP6 also binds and promotes assembly of the mature HIV-1 CA lattice.

Our results lead to the following model (Fig. 4): IP6 facilitates formation of the six-helix CA-SP1 bundle by binding to two rings of primary amines at Lys290 and Lys359, thereby neutralizing otherwise repulsive charges at the center of the HIV-1 Gag hexamer (Fig. 4c). Although other negatively-charged molecules can also bind this pocket, our data suggest that IP6 is the most potent in promoting assembly, likely because it has the most optimal binding geometry. Some 300–400 molecules of IP6 – one per hexamer – are incorporated into the virus particle as a structural component of the immature Gag shell (Fig. 4c). During virus maturation, proteolysis of Gag disrupts the 6HB, thus releasing IP6 and at the same time unmasking the Arg18 binding site in mature CA. IP6 then binds to this newly exposed site in CA (Fig. 4d), promoting formation of CA hexamers and in turn the mature CA lattice. This unprecedented involvement of a small molecule in two distinct steps in virus assembly, by binding to highly conserved sites, suggests strategies for possible therapeutic intervention in HIV-1 replication.

Methods

Protein purification.

DNA coding for HIV-1 Gag proteins were cloned into a His_6-SUMO vector[24]. The proteins were expressed in *E. coli* and purified using standard Ni^{2+} affinity chromatography followed by cleavage of the SUMO moiety by ULP1 protease. In brief, bacterial pellets were resuspended in buffer and lysed by sonication and cellular debris removed by centrifugation. The supernatant was filtered through a 0.2-μm filter, applied to a Ni^{2+} affinity resin, and eluted with imidazole. The eluted protein was dialyzed overnight in the presence of ULP1 protease, and subjected to Ni^{2+} chromatography a second time to remove the SUMO tag and ULP1 protease.

All proteins containing the NC domain were purified with additional steps for more stringent removal of nucleic acid. Following bacterial lysis and centrifugation, nucleic acid was precipitated by addition of 0.03% (v/v) polyethyleneimine followed by centrifugation.

Ammonium sulfate to 20% saturation was added to the resulting supernatant, and the precipitate was resuspended in buffer (20 mM Tris-HCl, pH 8, 100 mM NaCl, 2 mM TCEP (tris(2-carboxyethyl)phosphine), 5 μM $ZnCl_2$). The protein was then purified by anion exchange and Ni^{2+} chromatography as above. All purification steps were performed at 4 °C or on ice. All of the final purified proteins, at concentrations of 2–5 mg/mL and having A_{260}/A_{280} ratios of <0.6, were flash-frozen in liquid nitrogen and stored at −80 °C.

In vitro assembly.

Assembly of *s*-CANC VLPs was performed by dialyzing 50 μM protein against buffer (50 mM MES, pH 6 or 50 mM Tris-HCl, pH 8, 100 mM NaCl, 5 μM $ZnCl_2$, 2 mM TCEP) with a single-stranded 50-mer oligonucleotide (GT_{25}) at a 1:5 molar ratio of oligo to protein for 4 h at 4 °C. All reactions were adjusted to a final volume of 100 μL with buffer following dialysis. Working stocks of 10 mM inositol phosphates were made fresh (IP6, TCI cat# P0409; IP3-IP5, Cayman Chemical cat#s IP3–60960, IP4–60980, and IP5–10009851) with the pH adjusted to 6.0 with NaOH, and added both to the assembly reaction and dialysis buffer. Both *s*-CASP1 and CA_{CTD}SP1 assembly reactions were performed as described for *s*-CANC but with 500 μM protein and 500 μM IP6. Mature CA assembly was performed by dilution into buffer (50 mM MES, pH 6, 100 mM NaCl) to 250 μM final concentration in the presence of increasing amounts of IP6. Note that under these low-salt conditions, HIV-1 CA does not spontaneously assemble efficiently. The mature reactions were diluted 1:10 prior to spotting on EM grids. All VLP assemblies were visualized by EM negative staining with uranyl acetate. Quantification was performed by counting particles on at least five images from at least two different assembly reactions. Box plot; center lines show the medians; box limits indicate the 25th and 75th percentiles as determined by R software; whiskers extend to minimum and maximum values.

CRISPR knockout.

The lentiCRISPR v2 vector was a gift from Feng Zhang (Addgene plasmid # 52961)[26]. The VSV-G expression vector[27] was obtained through the NIH AIDS Research and Reference Reagent Program. HEK293FT cells were purchased from Invitrogen. Cell lines were tested for, and showed no mycoplasma contamination. The plasmid v906 is an HIV-1 NL4–3 derived provirus lacking Vpr, Vif, Env, and containing CMV GFP in place of Nef. The construct has several silent restriction sites added to the CA domain of Gag for cloning purposes. The IPPK-targeted guide RNA (5'-`AACAGCGCTGCGTCGTGCTG`-3') was cloned into lentiCRISPR v2, which was then used to transduce 293FT cells, followed by selection with puromycin at 1 μg/mL. Clonal isolates of the stably transduced cells were obtained by limiting dilution. To confirm the knockout, genomic DNA was isolated from clonal isolates using the DNeasy blood and tissue kit (Qiagen) following the manufacturer's protocol. The guide RNA target sequence was amplified from genomic DNA using primers 5'-`GAAATGTGTGCCACTGTGTTTA`-3' and 5'-`ATGATGGACACACCACTTTCT`-3'. The PCR product was directly sequenced.

Infectivity assays.

Equivalent numbers of 293FT WT or IPPK KO cells were plated in 35-mm dishes and transfected with 900 ng of v906 and 100 ng of VSV-G. Media was collected two days post-transfection and frozen at −80 °C to lyse cells in the supernatant. Thawed supernatants were centrifuged at 1,500*g* for 5 min to remove cellular debris. Infections were performed in fresh 293FT cells. Cells were collected two days later, fixed with 4% paraformaldehyde, and analyzed for GFP expression using an Accuri C6 flow cytometer.

Two-dimensional (2D) crystallography.

CA_{CTD}SP1 2D crystals were produced by incubating 0.8 mM protein with 0.8 mM IP6 at room temperature for 30 min. Samples were placed on a carbon-coated grid, washed with 0.1 M KCl, blotted to near dryness and flash frozen by plunging in liquid ethane. Low-dose images were collected on a Tecnai F20 equipped with 4k×4k Ultrascan CCD camera (Gatan) under low electron-dose conditions (~20 e-/A^2). Images were converted to MRC format and manual indexing, unbending, and corrections for CTF were performed with 2dx[28].

X-ray crystallography.

Purified CA_{CTD}SP1 protein (stock = 4.5 mg/mL) was mixed with equal volume of IP6 (stock = 1.4 mM) and incubated briefly at room temperature. Crystals were formed by the vapor diffusion method in sitting drops containing a 1:1 ratio of the protein/IP6 mix and precipitant (0.2 M NaCl, 20% PEG 3,350, 0.1 M Bis-Tris, pH 5.35). Hexagonal plate crystals grew after 2 days of incubation at 17 °C. Crystals were cryoprotected in 25% ethylene glycol and flash-frozen in liquid nitrogen. Diffraction data were collected at the Advanced Photon Source beamline 22-ID and were indexed and scaled with HKL2000[29]. The structure was solved by molecular replacement using as search model one monomer of the previously reported CA_{CTD}SP1 hexamer structure (PDB 5I4T)[3], with Lys290 and Lys359 sidechains truncated at Cα. Refinement and model building were performed using the PHENIX suite of programs[30] and Coot[31]. Refinement of the protein was first completed prior to modeling the IP6 and Lys290/Lys359 sidechain densities. The IP6 density was unambiguously identified from mF_o-DF_c difference maps, and the interpretation that the density was due to bound IP6 was further supported by comparison with difference maps from our previously reported CA_{CTD}SP1 structure in the absence of IP6[3]. Given the resolution of the data and crystallographic averaging of the ligand density, we assumed that the bound IP6 was in the *myo* conformation and refined the ligand as a rigid body with 1/6 occupancy. Only weak residual difference densities were observed after this treatment, suggesting that the modeled IP6 conformation was a reasonable interpretation of the data.

Disulfide-stabilized CA A14C/E45C/W184A/M185A was prepared as described previously[32,33]. IP6-containing samples were prepared for crystallization as described for CA_{CTD}SP1, except that the protein stock concentration in this case was 10 mg/mL. P6 crystals were obtained in precipitant containing 2% Tacsimate, 14% PEG 8,000, 0.1 M Tris, pH 8.4, whereas P212121 crystals were obtained in 8% PEG 8,000, 0.1 M Tris, pH 8.2. Data were collected at Advanced Photon Source beamline 22-BM (P6 form) or 22-ID (P212121 form) and processed with HKL2000[29]. The crystals were isomorphous with previously deposited structures solved in the absence of IP6 (PDB 3H47 and 3H4E)[32], and so initial

refinement was through rigid body placement of the deposited coordinates (with Arg150 sidechains and waters removed). Refinement of protein-only models were first completed prior to modeling the IP6 and Arg150 sidechain densities. As with the immature hexamer, IP6 densities were unambiguously identified by mF_o-DF_c difference maps and by difference density comparisons of CA hexamers crystallized with and without IP6. The IP6 densities in the mature hexamers were modeled as follows. For the P6 crystal form, a single well-defined IP6 density was found inside the β-hairpin chamber (Fig. 3c-e). As in the case of the immature hexamer, the ligand density was also 6-fold symmetric due to crystallographic averaging, but in this case indicated at least two binding modes, one with the axial phosphate pointing away from the Arg18 ring and a second pointing towards the ring. Two IP6 molecules were therefore docked into the density, again in the *myo* form and refined as rigid bodies with 1/12 occupancy (Fig. 3e). Again, only weak residual difference densities were observed after this treatment, suggesting that the modeled IP6 conformations were reasonable interpretations of the data. For the P212121 form, IP6 densities were observed on both sides of the Arg18 ring (there were 2 hexamers in the asymmetric unit and so we observed 4 density features) (Extended Data Fig. 8). These were modeled by docking *myo*-IP6 in one or two configurations that appeared most consistent with the local density distribution, and then refined as rigid bodies with appropriate occupancy. In this case, significant residual difference densities were observed at the ligand positions after refinement, indicating that additional binding modes were possible. However, we did not attempt to model these multiple overlapping binding modes. The P6 form crystallized in the presence of Tacsimate (Hampton Scientific), which is a mixture of organic carboxylic acids. The excess of negatively charged precipitant therefore appears to have inhibited binding of IP6 below the Arg18 ring; this can be reasonably interpreted to mean that IP6 has greater affinity for the site enclosed by the β-hairpins. The P212121 form crystallized in the absence of Tacsimate, allowing IP6 binding on both sides of the Arg18 ring.

Statistics for all three crystal structures are reported in Extended Data Table 1. Structure visualizations and images were made by using PyMol (Schrödinger Scientific).

Molecular dynamics simulations.

The structure of the IP6-bound $CA_{CTD}SP1$ hexamer was used to derive bound and unbound $CA_{CTD}SP1$ models. The IPs and mellitic acid molecules were placed in the central pore of the hexamer between K290 and K359 rings in the corresponding models by aligning the carbons present in the central cyclic ring. All models were then solvated with TIP3P water[34] and the salt concentration was set to 150 mM NaCl. Sixteen chloride molecules and twenty-three sodium ions were placed near the hexamer using the CIONIZE plugin in VMD[35] to minimize the electrostatic potential. The resulting $CA_{CTD}SP1$ models each contained a total of 30,000 atoms.

After model building, the systems were initially subjected to minimization in two stages, both using the conjugated gradient algorithm[36] with linear searching[37]. Each stage consisted off 10,000 steps of energy minimization. During the first stage, only water molecules and ions were free to move, while the protein and IP molecules, if any, were fixed. In the second stage, the backbone atoms of the protein were restrained with a force constant of 10.0

Kcal/mol Å^2. Convergence of the minimizations were confirmed once the variances of gradients were not greater than 1 Kcal/mol Å. During thermalization the systems were heated from 50 K to 310 K in 20 K increments over 1 ns. Subsequently, the systems were equilibrated, while the backbone atoms of CA_{CTD}SP1 were restrained. The positional restraints were gradually released at a rate of 1.0 Kcal mol^{-1} Å^{-2} per 400 ps from 10.0 to 0.0 Kcal mol^{-1} Å^{-2}. NAMD 2.12[38] was employed during minimization/thermalization and equilibration steps.

Simulations of IP6-bound and unbound CA_{CTD}SP1 were then performed on the special purpose computer Anton2[39] in the Pittsburgh supercomputing center for 2 μs. The CHARMM 36m[40] force-field was employed for all simulations. Parameters for IP6 were derived by analogy following the CGENFF protocol[41]. During the simulation, the temperature (310 K) and pressure (1 atm) were maintained by employing the Multigrator integrator[42] and the simulation time-step was set to 2.5 fs/step, with short-range forces evaluated at every time step, and long-range electrostatics evaluated at every second time step. Short-range non-bonded interactions were cut off at 17 Å; long range electrostatics were calculated using the k-Gaussian Split Ewald method[43].

Simulations of CA_{CTD}SP1 bound to IP3, IP4, and IP5 were performed for 2 μs on TACC Stampede 2 using NAMD 2.12[38]. The molecular simulations were conducted under isothermal (310 K) and isobaric (1 atm) conditions, regulated by the Langevin thermostat[44] and the Nosé-Hoover Langevin piston[45-46], respectively. All bonds to hydrogen atoms were constrained with the SHAKE algorithm[47]. A timestep of 2 fs was employed for all simulations. Long-range electrostatics were calculated using the Particle-Mesh-Ewald method, as implemented in NAMD[38], with a cutoff of 1.2 nm. Full electrostatic interactions were calculated every two timesteps while nonbonded interactions were performed every time step.

Analysis of MD simulations.

Root-mean-square deviations (RMSDs) and root mean square fluctuations (RMSFs) of the Cα of the CA_{CTD}-SP1 hexamers were computed using the measure command in VMD[35]. Before RMSD and RMSF calculations, the structure of the hexamer was aligned to a common reference. RMSFs of each monomer in a central hexamer were calculated in order to obtain RMSF standard deviations of an entire hexamer.

Data availability.

Coordinates and structure factors are deposited at the PDB data base, under accession numbers 6BH5, 6BHT, and 6BHS. All other data are available from the authors on request; see author contributions for specific data sets.

Extended Data

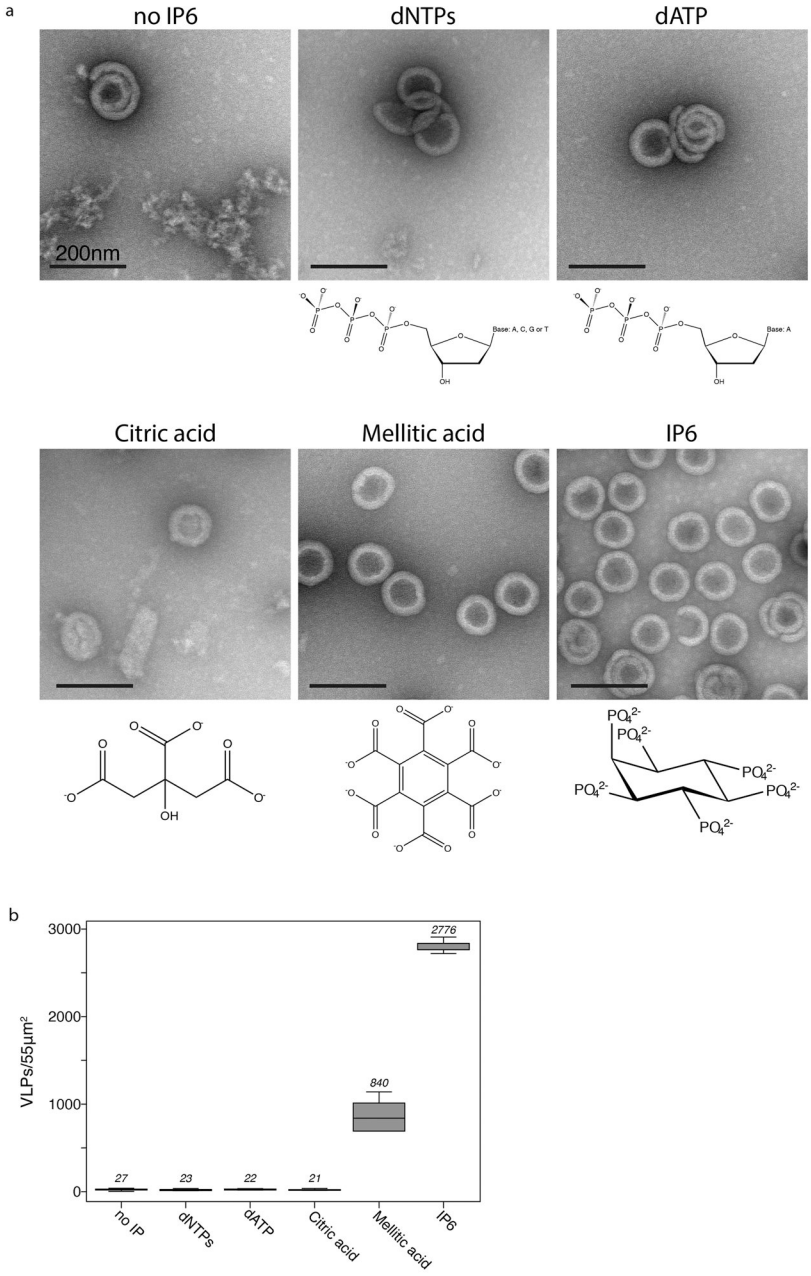

Extended Data Fig. 1 |. Effect of acidic molecules on immature *s*-CANC assembly.
a, Representative negative stain EM images. Scale bars, 200 nm. The experiment was repeated two times with similar results. **b**, Number of immature VLPs per 55 μm^2. n=5 and mean above box plots; center lines show the medians; box limits indicate the 25th and 75th percentiles as determined by R software; whiskers extend to minimum and maximum values.

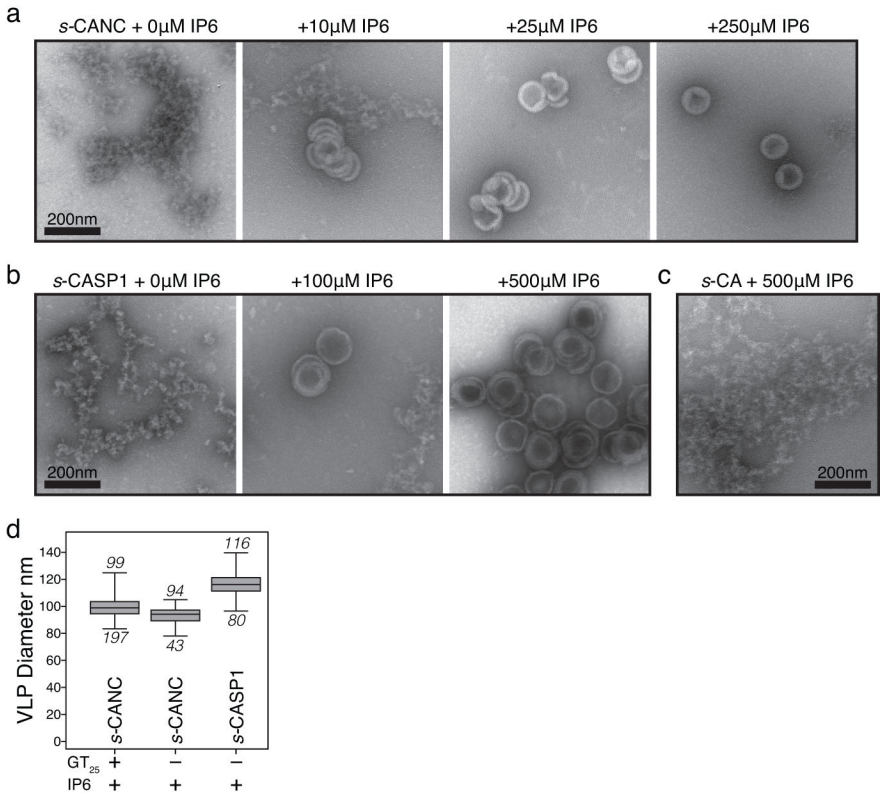

Extended Data Fig. 2 | *s*-CANC and *s*-CASP1 VLPs.

a-c, Representative negative stain EM images of *s*-CANC (a), *s*-CASP1 (b), and *s*-CA (c) proteins assembled in the absence of GT_{25} and in the presence of the indicated IP6 concentrations. Scale bars, 200 nm. **d**, Diameters of immature VLPs; mean diameter above plot; *n* below plot. Center lines show the medians; box limits indicate the 25th and 75th percentiles as determined by R software; whiskers extend to minimum and maximum values.

a

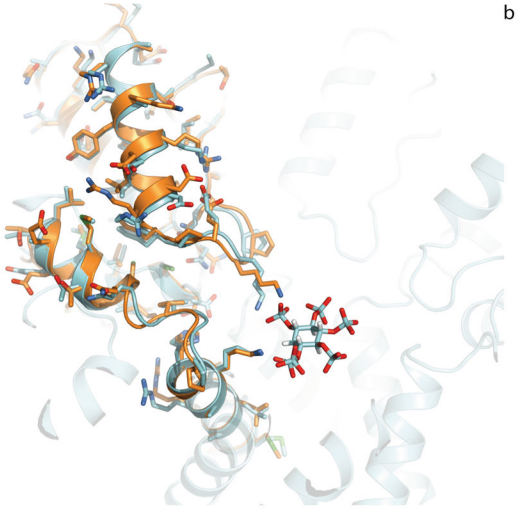

b

Selection	RMSD (Å)
full chain (624 atom pairs)	1.391
Cα (backbone, 89 atom pairs)	0.763
CA-SP1 (92 atom pairs)	1.397
K290& K359 (18 atom pairs)	1.299

c

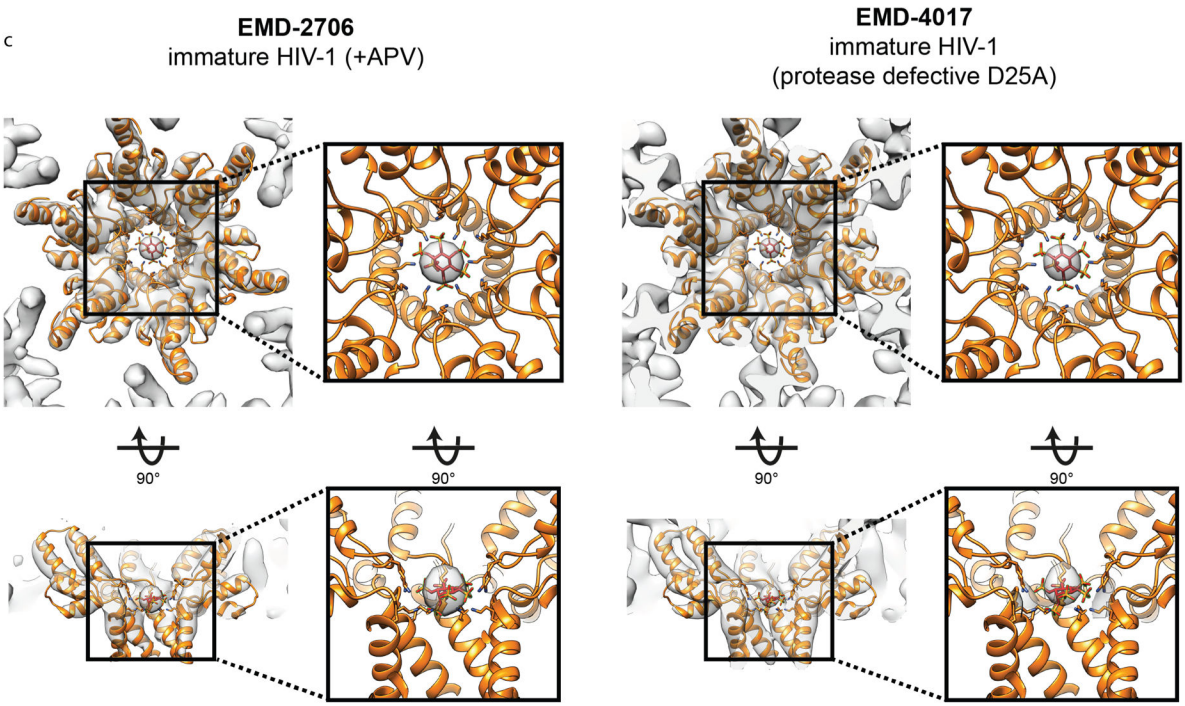

Extended Data Fig. 3 |. Comparison of the HIV-1 Gag cryoEM structure with the CA_{CTD}SP1/IP6 crystal structure.

a, The crystal structure of CA_{CTD}SP1 bound to IP6 (cyan) was superimposed on a previously described model of the CA-SP1 segment build into cryoEM densities of immature HIV-1 particles (PDB 5L93, orange[2]). Note the close correspondence in K359 rotamers, which were modeled independently in the two structures. For visualization purposes, only one of the six possible IP6 conformations is displayed. **b**, RMSD calculations of the crystal structure and PDB 5L93. For full-length (residues 149–237) and CA-SP1 (residues 223–237), the RMSDs were calculated only for the atoms that were modeled in both maps. In case a side chain was not modeled, the entire residue was omitted from the

calculation. The overall agreement of the models is very high, indicating that the crystal structure corresponds well with conformations found in the virus. **c**, The $CA_{CTD}SP1$ bound to IP6 (orange and red, respectively) was fitted into two previously published cryoEM densities[2] from VLPs collected from cells (EMD-2706 and EMD-4017). Both EM maps are shown at 8.8 Å, which is the resolution of the lower resolved map, EMD-2706. In the zoomed insets only the density corresponding to IP6 is shown. Matching of models and maps, and RMSD calculations were performed in Chimera.

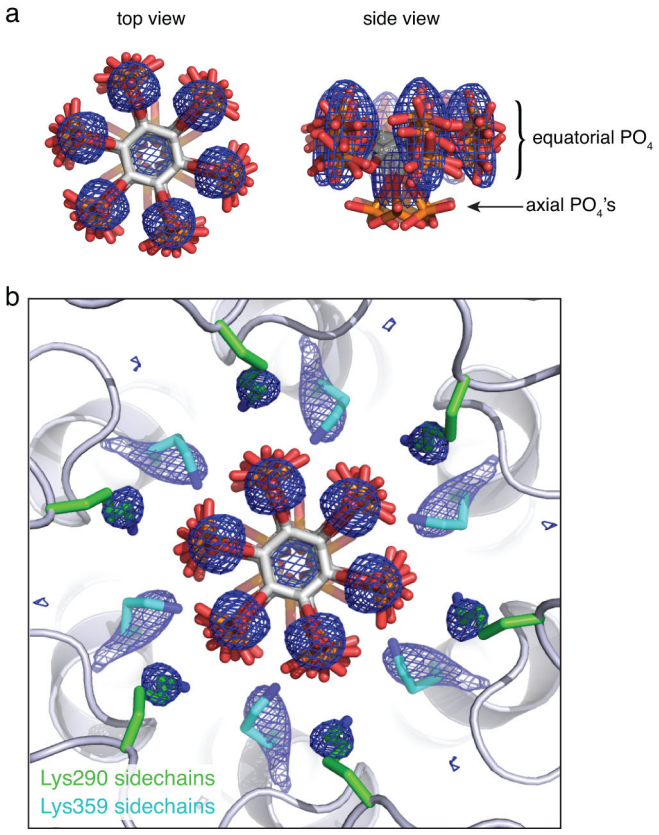

Extended Data Fig. 4 |. Interpretation of the IP6 density in the immature $CA_{CTD}SP1$ hexamer structure.

a, Top and side views of the unbiased mF_o-DF_c difference density (blue mesh, 2σ) ascribed to the bound IP6. Shown are six IP6 molecules docked in six rotationally equivalent positions, consistent with the six-fold rotational symmetric density. **b**, Top view of the docked IP6 molecules within the $CA_{CTD}SP1$ hexamer. Unbiased mF_o-DF_c difference densities (blue mesh) are also shown for both the bound IP6 and sidechains of Lys290 (green) and Lys359 (cyan). Density for Lys359 is more pronounced, which we interpret to mean that this residue adopts a more restricted range of rotamers for binding IP6.

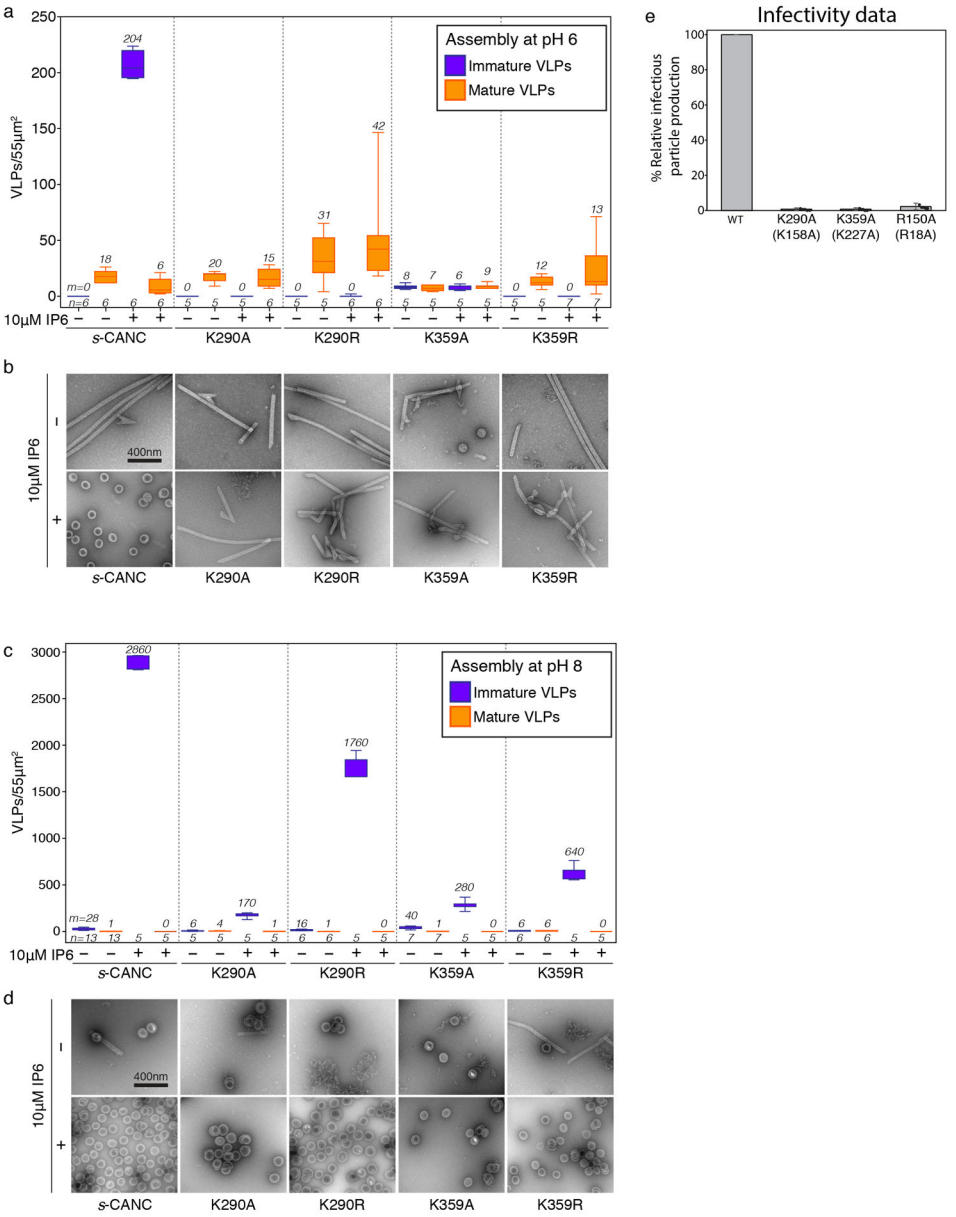

Extended Data Fig. 5 | Quantification of wild type and mutant HIV *s*-CANC assembly at pH 6 and 8.

a,c, Number of immature (purple) and mature (orange) VLPs per 55 μm^2 without (−) and with (+) 10 μM IP6 at pH 6 and pH 8. Mean above and *n* below box plots. Center lines show the medians; box limits indicate the 25th and 75th percentiles as determined by R software; whiskers extend to minimum and maximum values. **b,d**, Representative negative stain EM images of WT and mutant *s*-CANC assembly in the absence (−) and presence (+) of 10 μM IP6 at pH 6 and 8. Scale bar, 400 nm. Repeated three times with similar results. **e**, Infectivity relative to WT virus of IP6 binding residues mutated to alanine; CA residue numbering in parenthesis. Error bars represent standard deviation, individual data points represented as dots, *n* from four independent experiments.

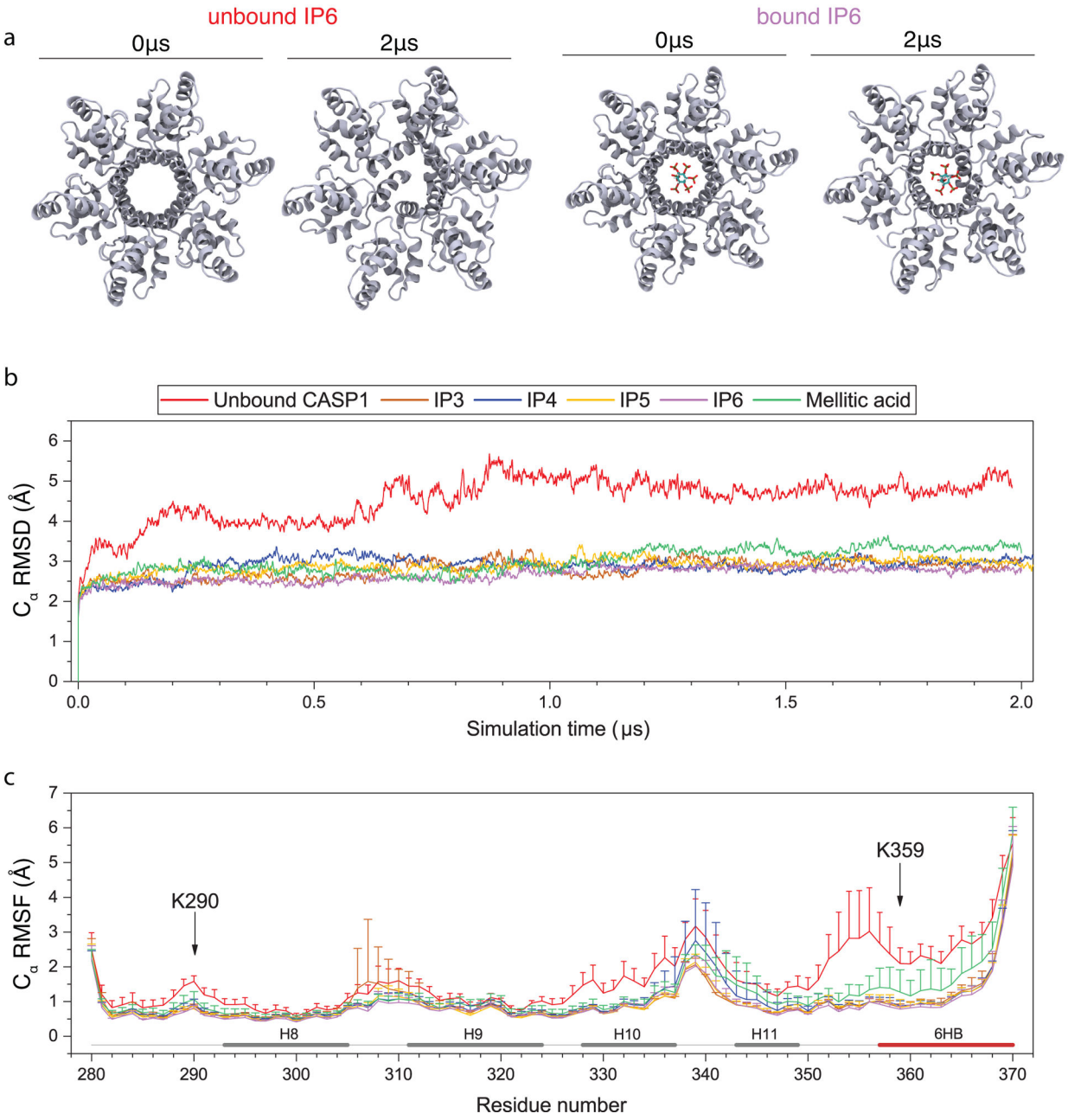

Extended Data Fig. 6 | IP6 modulates the stability of the 6HB.

a, Structural changes observed after 2 μs of molecular dynamics simulations of $CA_{CTD}SP1$ with and without bound IP6. **b**, RMSDs of the ligand-bound and unbound forms of $CA_{CTD}SP1$ hexamers. **c**, RMSFs of the central hexamer during the simulation. The RMSF was averaged over the six central monomers; dashed line shows the standard deviation for each residue.

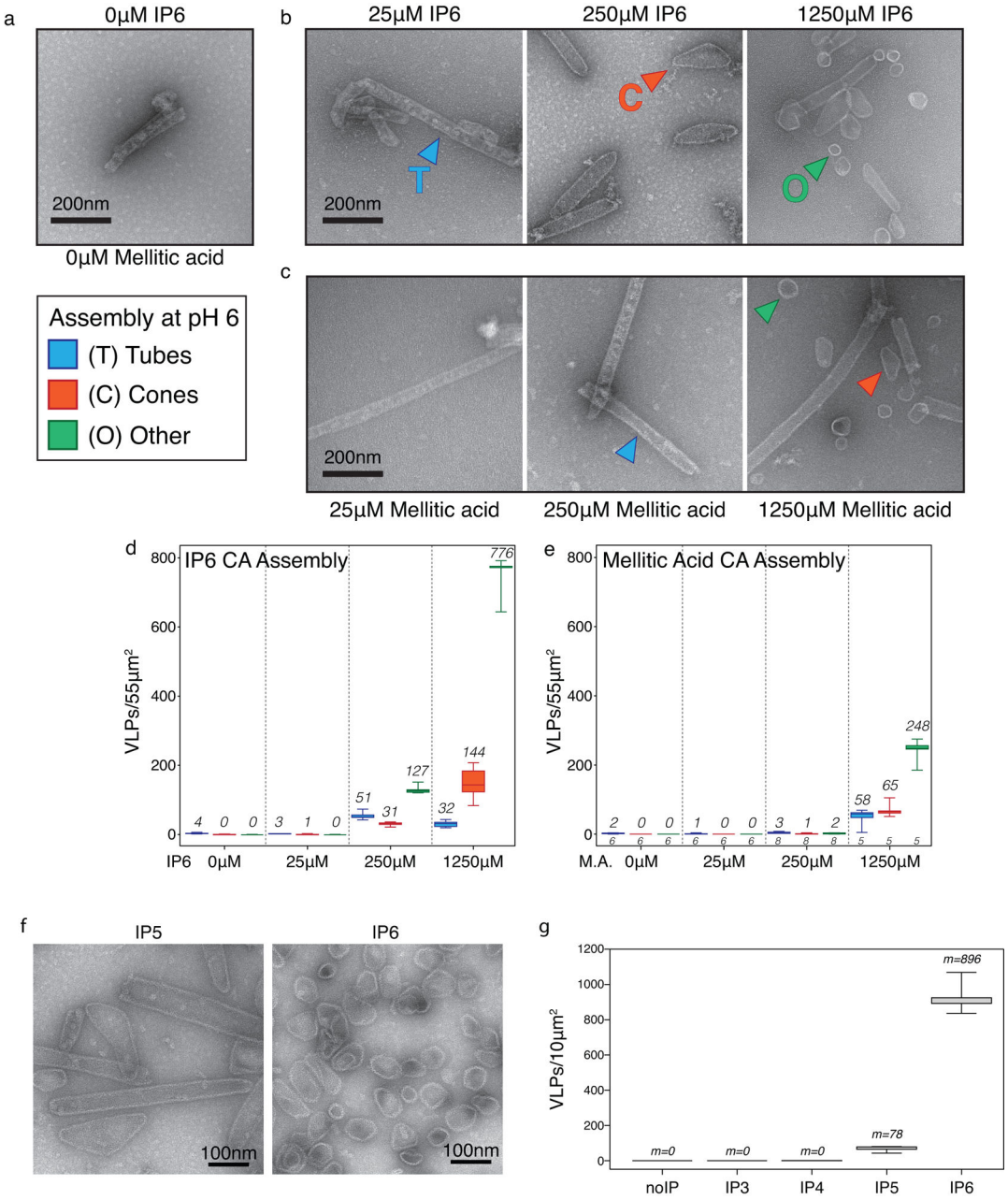

Extended Data Fig. 7 |. Quantification of mature HIV-1 CA assembly and VLP diameter at pH 6. **a**, Example of CA assembly in the absence of IP6 or mellitic acid. **b-c**, Representative negative stain EM images of assemblies induced by IP6 (b) and mellitic acid (c). Scale bars, 200 nm. Tubes (T), cones (C), and other (O) morphologies are marked by colored arrowheads. (a, b, c) Repeated four times with similar results. **d**, Number of CA assembled tubes (blue), cones (orange), and other (green) per 55 μm^2 at increasing IP6 concentrations. Mean above and n=5 **e**, Number of CA assembled tubes (blue), cones (orange), and other (green) per 55 μm^2 at increasing mellitic acid concentrations. Mean above and below box plots. **f**, Representative images of mature VLPs assembled with IP5 and IP6 at 50 mM NaCl. Scale bars, 100 nm. Repeated three times with similar results. **g**, Number of CA VLPs per

10 μm^2 without and with IP3, IP4, IP5, and IP6. Mean above and n=5. (d-e, g) Center lines show the medians; box limits indicate the 25th and 75th percentiles as determined by R software; whiskers extend to minimum and maximum values.

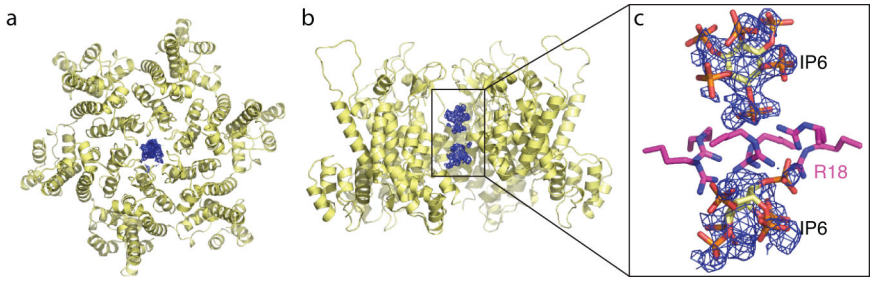

Extended Data Fig. 8 | Crystal structure of IP6 bound to the mature CA hexamer. **a,b**, Top view (a) and side view (b) of a second CA hexamer crystal structure (P212121 space group) showing the protein in yellow ribbons and unbiased mF_o-DF_c difference density in blue mesh, contoured at 2.5**σ**. **c**, Close-up view showing IP6 densities both above and below the ring of Arg18 residues (magenta).

Extended Data Table 1 |

Crystallographic statistics. Values in parentheses are for highest-resolution shell. Each structure was solved from data collected with 1 crystal.

	CA_{CTD}-SPI+IP6	CA^{CC1}+IP6	CA^{CC1}+IP6
Data collection			
Space group	P6	P6	P212121
Cell dimensions			
a, *b*, *c* (Å)	70.9,70.9,42.0	90.6,90.6,56.6	135.6,137.8,209.9
α, β, γ (°)	90,90,120	90,90,120	90,90,90
Resolution (Å)	50-2.90 (2.95-2.90)	50-1.98(2.03-1.98)	50-2.69 (2.74-2.69)
R_{merge}	0.16 (0.94)	0.16 (1.69)	0.06 (0.79)
$I/\sigma I$	10.3 (1.1)	15.2 (1.2)	13.1 (1.1)
Completeness (%)	96.3 (87.8)	100 (100)	99.3 (98.8)
Redundancy	8.1 (4.3)	11.0 (8.8)	3.8 (3.6)
Refinement			
Resolution (Å)	35.47-2.91	39.25-1.98 (2.12-1.98)	39.902.69 (2.97-2.69)
No. reflections	1,986	18,196 (2.660)	95,906 (2,545)
R_{work}/R_{free}	21.5/26.5	23.6/28.4 (28.0/32.4)	22.7/25.4 (30.3/35.5)
No. atoms			
Protein	668	1,641	19,621
IP6	36	72	144
Water	0	145	173
B-factors (Å^2)			
Protein	33.0	35.4	57.0
IP6	39.2	39.6	157.5

	CA_{CTD}-SPI+IP6	CA^{CC1}+IP6	CA^{CC1}+IP6
Water	n/a	35.9	31.0
R.m.s. deviations			
Bond lengths (Å)	0.005	0.005	0.003
Bond angles (°)	1.093	1.091	0.630

Supplementary Material

Refer to Web version on PubMed Central for supplementary material.

Acknowledgments.

The authors thank John Briggs for discussions and critical reading of the manuscript. This work was supported by the National Institutes of Health (NIH) grants R01-GM107013 (V.M.V), R01-GM105684 (G.W.F.), P30-GM110758 and P50-GM082251 (J.R.P.), R01-AI129678 (O.P. and B.K.G.-P.), U54-GM103297 (O.P.), and R01-GM110776 (M.C.J.). F.K.M.S. was supported by Deutsche Forschungsgemeinschaft grant BR 3635/2–1 awarded to John A. G. Briggs. J.M.W. was supported by NIH postdoctoral fellowship grant F32-GM115007. Anton computer time was provided by the Pittsburgh Supercomputing Center (PSC) through NIH grant R01-GM116961. The Anton machine at PSC was generously made available by D. E. Shaw Research. This work used the Extreme Science and Engineering Discovery Environment (XSEDE), which is supported by National Science Foundation (NSF) grant number OCI-1053575. Specifically, it used the Bridges system, which is supported at PSC by NSF award number ACI-1445606.

References

1. Gross I et al. A conformational switch controlling HIV-1 morphogenesis. EMBO J 19, 103–113 (2000). [PubMed: 10619849]
2. Schur FK et al. An atomic model of HIV-1 capsid-SP1 reveals structures regulating assembly and maturation. Science 353, 506–508 (2016). [PubMed: 27417497]
3. Wagner JM et al. Crystal structure of an HIV assembly and maturation switch. eLife 5, e17063 (2016). [PubMed: 27416583]
4. Keller PW, Adamson CS, Heymann JB, Freed EO & Steven AC HIV-1 maturation inhibitor bevirimat stabilizes the immature Gag lattice. J. Virol 85, 1420–1428 (2011). [PubMed: 21106735]
5. Wang M et al. Quenching protein dynamics interferes with HIV capsid maturation. Nat. Commun 8, 1779 (2017). [PubMed: 29176596]
6. Letcher AJ, Schell MJ & Irvine RF Do mammals make all their own inositol hexakisphosphate? Biochem. J 416, 263–270 (2008). [PubMed: 18684107]
7. Campbell S et al. Modulation of HIV-like particle assembly in vitro by inositol phosphates. Proc. Natl. Acad. Sci. U.S.A 98, 10875–10879 (2001). [PubMed: 11526217]
8. Datta SAK et al. Interactions between HIV-1 Gag molecules in solution: an inositol phosphate-mediated switch. J. Mol. Biol 365, 799–811 (2007). [PubMed: 17098251]
9. Munro JB et al. A conformational transition observed in single HIV-1 Gag molecules during *in vitro* assembly of virus-like particles. J. Virol 88, 3577–3585 (2014). [PubMed: 24403576]
10. von Schwedler UK et al. Proteolytic refolding of the HIV-1 capsid protein amino-terminus facilitates viral core assembly. EMBO J 17, 1555–1568 (1998). [PubMed: 9501077]
11. Accola MA, Strack B & Göttlinger HG Efficient particle production by minimal Gag constructs which retain the carboxy-terminal domain of human immunodeficiency virus type 1 capsid-p2 and a late assembly domain. J. Virol 74, 5395–5402 (2000). [PubMed: 10823843]
12. Loewus FA & Murthy PPN *Myo*-inositol metabolism in plants. Plant Sci. 150, 1–19 (2000).
13. van Galen J et al. Interaction of GAPR-1 with lipid bilayers is regulated by alternative homodimerization. Biochim. Biophys. Acta 1818, 2175–2183 (2012). [PubMed: 22560898]

14. Ouyang ZQ, Zheng G, Tomchick DR, Luo XL & Yu HT Structural basis and IP6 requirement for Pds5-dependent cohesin dynamics. Mol. Cell 62, 248–259 (2016). [PubMed: 26971492]
15. Macbeth MR et al. Inositol hexakisphosphate is bound in the ADAR2 core and required for RNA editing. Science 309, 1534–1539 (2005). [PubMed: 16141067]
16. Chang YF, Wang SM, Huang KJ & Wang CT Mutations in capsid major homology region affect assembly and membrane affinity of HIV-1 Gag. J. Mol. Biol 370, 585–597 (2007). [PubMed: 17532005]
17. von Schwedler UK, Stray KM, Garrus JE & Sundquist WI Functional surfaces of the human immunodeficiency virus type 1 capsid protein. J. Virol 77, 5439–5450 (2003). [PubMed: 12692245]
18. Melamed D et al. The conserved carboxy-terminus of the capsid domain of human immunodeficiency virus type 1 Gag protein is important for virion assembly and release. J. Virol 78, 9675–9688 (2004). [PubMed: 15331700]
19. Rihn S et al. Extreme genetic fragility of the HIV-1 capsid. PLoS Pathog. 9, e1003461 (2013). [PubMed: 23818857]
20. Ganser-Pornillos BK, von Schwedler UK, Stray KM, Aiken C & Sundquist WI Assembly properties of the human immunodeficiency virus type 1 CA protein. J. Virol 78, 2545–2552 (2004). [PubMed: 14963157]
21. Ganser-Pornillos BK, Cheng A & Yeager M Structure of full-length HIV-1 CA: a model for the mature capsid lattice. Cell 131, 70–79 (2007). [PubMed: 17923088]
22. Pornillos O, Ganser-Pornillos BK & Yeager M Atomic-level modelling of the HIV capsid. Nature 469, 424–427 (2011). [PubMed: 21248851]
23. Jacques DA et al. HIV-1 uses dynamic capsid pores to import nucleotides and fuel encapsidated DNA synthesis. Nature 536, 349–353 (2016). [PubMed: 27509857]
24. Malakhov MP et al. SUMO fusions and SUMO-specific protease for efficient expression and purification of proteins. J. Struct. Funct. Genomics 5, 75–86 (2004). [PubMed: 15263846]
25. R Core Team. R: A language and environment for statistical computing. (R Foundation for Statistical Computing, Vienna, Austria, 2013).
26. Sanjana NE, Shalem O & Zhang F Improved vectors and genome-wide libraries for CRISPR screening. Nat. Methods 11, 783–784 (2014). [PubMed: 25075903]
27. Chang LJ, Urlacher V, Iwakuma T, Cui Y & Zucali J Efficacy and safety analyses of a recombinant human immunodeficiency virus type 1 derived vector system. Gene Ther 6, 715–728 (1999). [PubMed: 10505094]
28. Gipson B, Zeng X, Zhang ZY & Stahlberg H 2dx – user-friendly image processing for 2D crystals. J. Struct. Biol 157, 64–72 (2007). [PubMed: 17055742]
29. Otwinowski Z & Minor W Processing of X-ray diffraction data collected in oscillation mode. Methods Enzymol. 276, 307–326 (1997).
30. Adams PD et al. PHENIX: a comprehensive Python-based system for macromolecular structure solution. Acta Crystallogr. D Biol. Crystallogr 66, 213–221 (2010). [PubMed: 20124702]
31. Emsley P, Lohkamp B, Scott WG & Cowtan K Features and development of Coot. Acta Crystallogr. D Biol. Crystallogr 66, 486–501 (2010). [PubMed: 20383002]
32. Pornillos O et al. X-Ray structures of the hexameric building block of the HIV capsid. Cell 137, 1282–1292 (2009). [PubMed: 19523676]
33. Pornillos O, Ganser-Pornillos BK, Banumathi S, Hua YZ & Yeager M Disulfide bond stabilization of the hexameric capsomer of human immunodeficiency virus. J. Mol. Biol 401, 985–995 (2010). [PubMed: 20600115]
34. Jorgensen WL & Jenson C Temperature dependence of TIP3P, SPC, and TIP4P water from NPT Monte Carlo simulations: seeking temperatures of maximum density. J. Comput. Chem 19, 1179–1186 (1998).
35. Humphrey W, Dalke A & Schulten K VMD: Visual molecular dynamics. J. Mol. Graphics 14, 33–38 (1996).
36. Fletcher R & Reeves CM Function minimization by conjugate gradients. Comput. J 7, 149–154 (1964).

37. Sun W & Yuan Y-X Optimization Theory and Methods: Nonlinear Programming. (Springer US, 2006)
38. Phillips JC et al. Scalable molecular dynamics with NAMD. J. Comput. Chem 26, 1781–1802 (2005). [PubMed: 16222654]
39. Shaw DE. Proceedings of the International Conference for High Performance Computing, Networking, Storage and Analysis; IEEE Press; New Orleans, Louisana. 2014. 41–53.
40. Best RB et al. Optimization of the additive CHARMM all-atom protein force field targeting improved sampling of the backbone ϕ, ψ and side-chain $\chi 1$ and $\chi 2$ dihedral angles. J. Chem. Theory Comput 8, 3257–3273 (2012). [PubMed: 23341755]
41. Vanommeslaeghe K et al. CHARMM general force field: a force field for drug-like molecules compatible with the CHARMM all-atom additive biological force fields. J. Comput. Chem 31, 671–690 (2010). [PubMed: 19575467]
42. Lippert RA et al. Accurate and efficient integration for molecular dynamics simulations at constant temperature and pressure. J. Chem. Phys 139, 164106 (2013). [PubMed: 24182003]
43. Shan Y, Klepeis JL, Eastwood MP, Dror RO & Shaw DE Gaussian split Ewald: a fast Ewald mesh method for molecular simulation. J. Chem. Phys 122, 054101 (2005).
44. Berendsen HJC, Postma JPM, Vangunsteren WF, Dinola A & Haak JR Molecular dynamics with coupling to an external bath. J. Chem. Phys 81, 3684–3690 (1984).
45. Martyna GJ, Tobias DJ & Klein ML Constant pressure molecular dynamics algorithms. J. Chem. Phys 101, 4177–4189 (1994).
46. Feller SE, Zhang YH, Pastor RW & Brooks BR, Constant pressure molecular dynamics simulation – the Langevin Piston Method. J. Chem. Phys 103, 4613–4621 (1995).
47. Ryckaert J-P, Ciccotti G & Berendsen HJ Numerical integration of the cartesian equations of motion of a system with constraints: molecular dynamics of *n*-alkanes. J. Comput. Phys 23, 327–341 (1977).

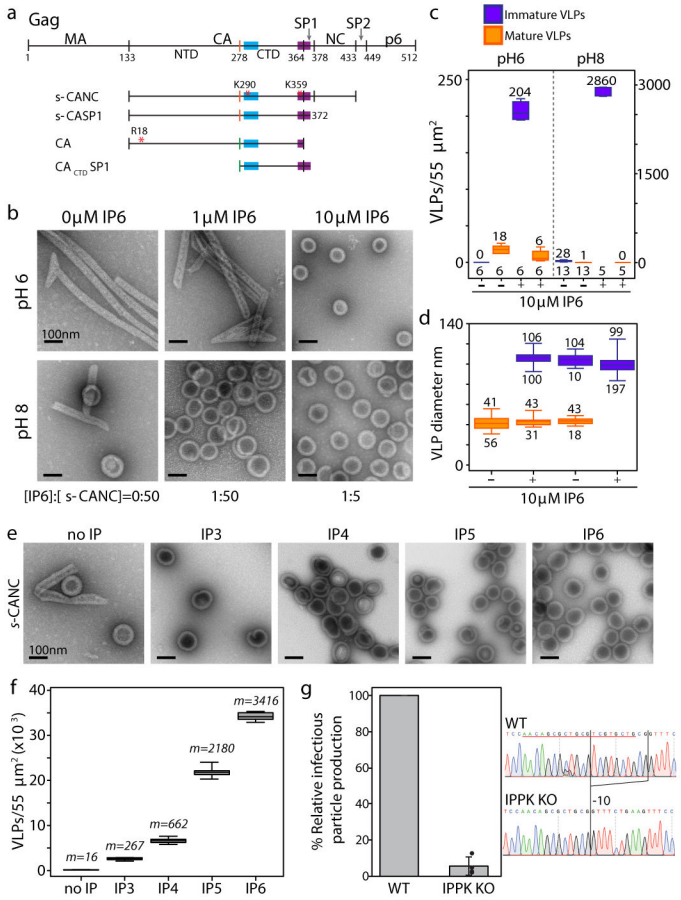

Fig. 1 |. IP6 induces assembly of HIV-1 Gag *in vitro*.

a, Map of the HIV-1 Gag protein, indicating the MA, CA, NC, and p6 domains, and spacer peptides SP1 and SP2. Gag-derived constructs used in this study are shown underneath. Blue bar, major homology region (MHR); purple bar, SP1 helix; NTD and CTD, N-terminal and C-terminal domains of CA; R18, K290, and K359, locations of mutations; N372, C-terminal residue of the *s*-CASP1 and $CA_{CTD}SP1$ constructs. **b**, Negative stain EM images of mature and immature VLPs formed by *s*-CANC (50 μM) at pH 6 and pH 8 in the absence or presence of the indicated molar ratios of IP6 (0–10 μM). Scale bars, 100 nm. **c**, Number of VLPs per 55/μm^2 without (−) and with (+) 10μM IP6 at pH 6 and pH 8; *n* below and mean above box plots. The experiment was repeated three times with similar results. **d**, Diameters of immature and mature VLPs; *n* below and mean above box plots. **e**, Representative images of *s*-CANC VLPs assembled at pH 8 in the absence and presence of IP3, IP4, IP5, and IP6. Scale bars, 100 nm. The experiment was repeated two times with similar results. **f**, Number of VLPs per 55/μm^2 without and with 10 μM IP3-IP6; *n*=5 and mean above box plots **g**, Parallel transfections of 293FT wildtype (WT) and IPPK KO were performed with a VSV-G-pseudotyped HIV-1 provirus containing GFP, and infectivity was measured on WT 293T cells. Graphs show average and standard deviations of 4 independent experiments; dots show individual data points. Right panels show sequences of total PCR products of the guide RNA target sites from WT and KO cells; guide RNA sequence is underlined in red. (**c**, **d**, **f**).

Center lines show the medians; box limits indicate the 25th and 75th percentiles as determined by R software; whiskers extend to minimum and maximum values.

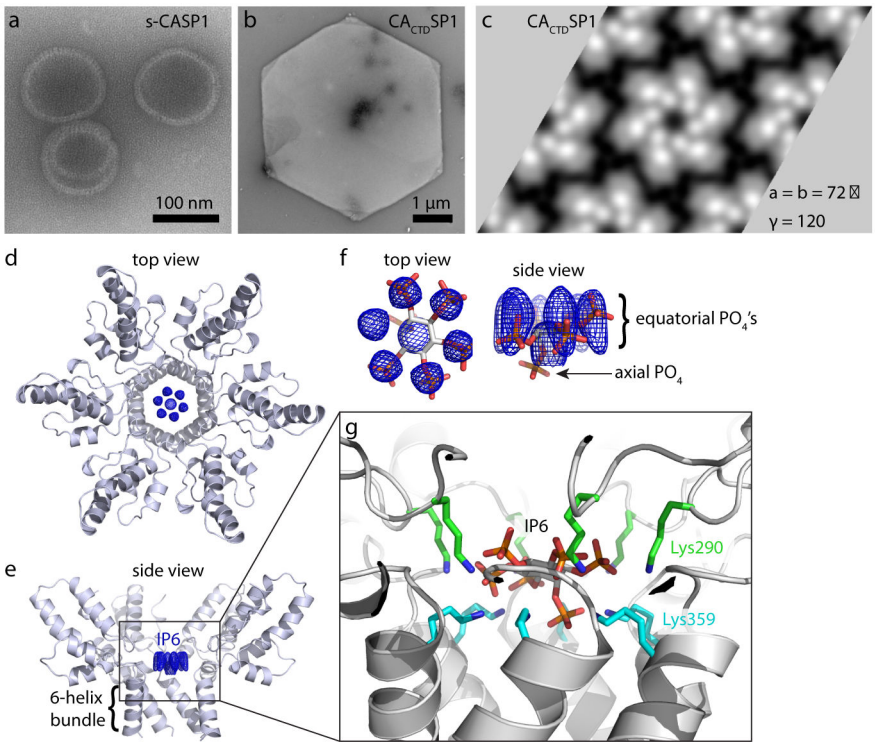

Fig. 2 | IP6 interacts with Lys290 and Lys359 in the immature HIV-1 Gag hexamer.

a, IP6-induced assembly of *s*-CASP1 into immature VLPs. The experiment was repeated four times with similar results. **b**, IP6-induced assembly of $CA_{CTD}SP1$ into flat micro-crystals. The experiment was repeated six times with similar results. **c**, 2D cryoEM projection map of a micro-crystal. Images of multiple crystals were collected during two rounds of data collection from separate assembly reactions and all crystals had similar unit cells. Two individual crystals had single layer regions and could be further processed. These crystals generated similar maps. **d-e**, Top view (d) and side view (e) of the $CA_{CTD}SP1$ hexamer crystal structure showing the protein in gray ribbons and unbiased mF_o-DF_c difference density in blue mesh, contoured at 2σ. **f**, Top and side views of IP6 in its *myo* configuration, docked into the difference density as a rigid body in one of six rotationally equivalent orientations. All six binding modes are shown in Extended Data Fig. 4a. **g**, Side view of the two rings of Lys290 (green) and Lys359 (cyan) with bound IP6 in the middle. Densities were omitted for clarity, and are shown in Extended Data Fig. 4b.

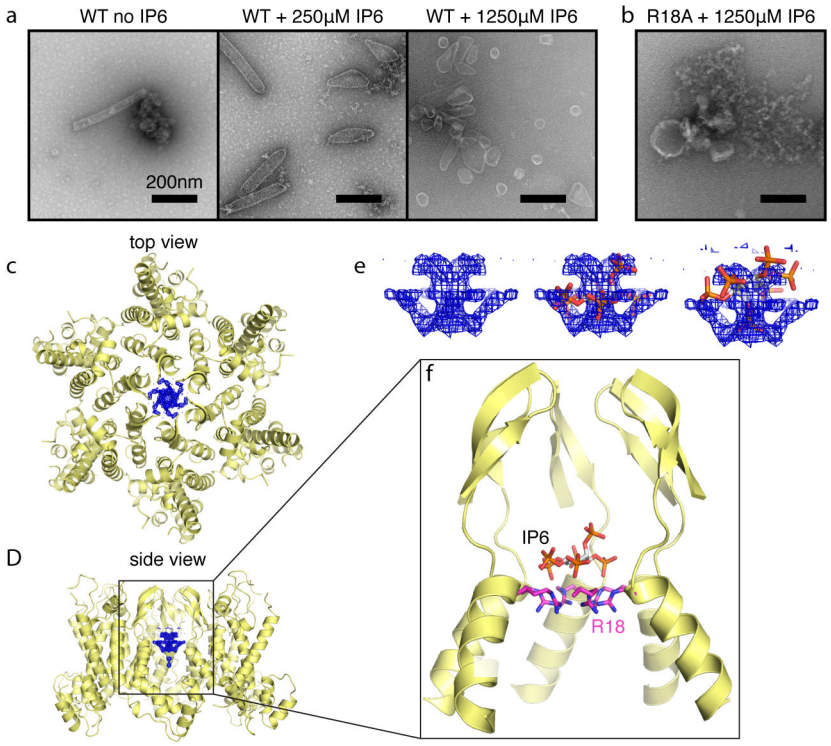

Fig. 3 |. IP6 induces mature CA assembly by interacting with Arg18.

a, Representative negative stain images of mature CA assemblies at pH 6 and 100 mM NaCl with increasing IP6 concentrations (0–1,250 μM). The experiment was repeated five times with similar results. **b**, Representative image of failed CA R18A assembly even in the presence of 1,250 μM IP6. The experiment was repeated three times with similar results. **c-d**, Top view (c) and side view (d) of a CA hexamer crystal structure showing the protein in yellow ribbons and unbiased mF_o-DF_c difference density in blue mesh, contoured at 2.2**σ**. **e**, Side views *myo*-IP6 docked into the difference density in two possible binding modes. **f**, Illustration of a single IP6 molecule bound within a chamber enclosed by the N-terminal β-hairpins and the Arg18 ring (magenta). In a second crystal form, IP6 densities were observed both above and below the Arg18 ring (Extended Data Fig. 8).

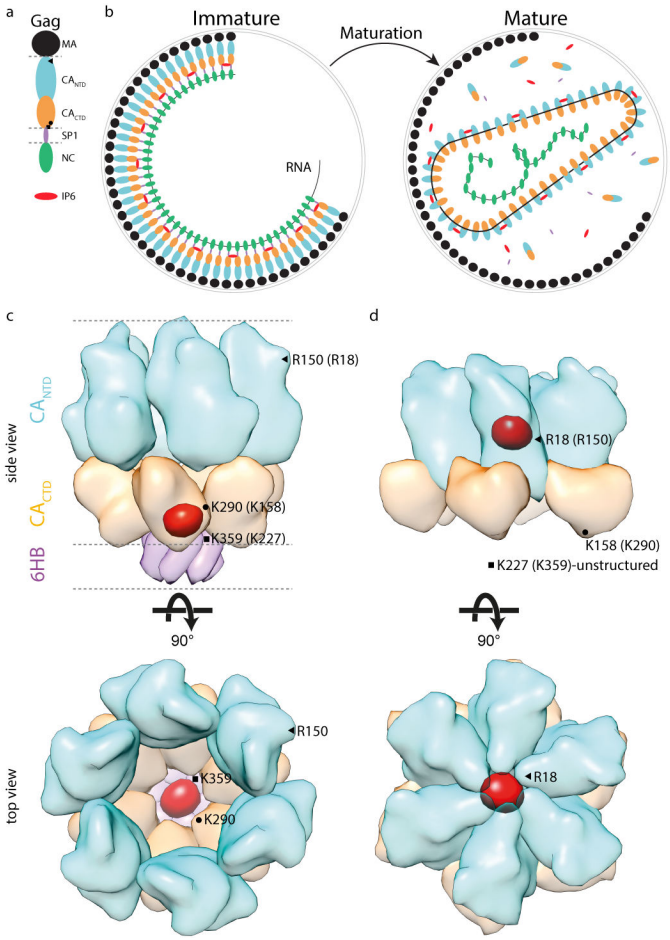

Fig. 4 |. Model.

a, Diagram of HIV-1 Gag, with the indicated positions of R150 (triangle; R18 in mature CA), K290 (circle; K158 in mature CA), K359 (square; K227 in mature CA). Dotted lines indicate protease cleavage sites. **b**, Diagram of Gag organization in immature virions (left). Following cleavage of Gag by protease (maturation), CA re-organizes to form a mature core around viral RNA (right). **c-d**, Surface representations of the CASP1 and CA hexamers in the immature and mature virus, respectively, with IP6 shown in its binding sites. The dramatic rearrangement of CA upon maturation is evident, as is the change of the IP6 binding site in immature and mature viruses. CA_{NTD}, blue; CA_{CTD}, orange; 6HB, purple; IP6, red.